Research Article | Vol. 11, No. 5 / 1 May 2020 / Biomedical Optics Express 2806

Biomedical Optics EXPRESS

Lensless microscopy platform for single cell and tissue visualization

RAMONA CORMAN,[1,2] WILLEM BOUTU,[1] ANNA CAMPALANS,[3] PABLO RADICELLA,[3] JOANA DUARTE,[1] MARIA KHOLODTSOVA,[1] LAURE BALLY-CUIF,[4] NICOLAS DRAY,[4] FABRICE HARMS,[2] GUILLAUME DOVILLAIRE,[2] SAMUEL BUCOURT,[2] AND HAMED MERDJI[1,*]

[1] *Université Paris-Saclay, CEA, CNRS, LIDYL, 91191, Gif-sur-Yvette, France*
[2] *Imagine Optic, 91400 Orsay, France*
[3] *CEA, Institute of Cellular and Molecular Radiobiology, Université de Paris and Université Paris-Saclay, Fontenay-aux-Roses, France*
[4] *Institut Pasteur, Dept Developmental and Stem Cell Biology, CNRS UMR3738, Paris, France*
[*] *hamed.merdji@cea.fr*

Abstract: Today, 3D imaging techniques are emerging, not only as a new tool in early drug discovery but also for the development of potential therapeutics to treat disease. Particular efforts are directed towards in vivo physiology to avoid perturbing the system under study. Here, we assess non-invasive 3D lensless imaging and its impact on cell behavior and analysis. We test our concept on various bio-applications and present here the first results. The microscopy platform based on in-holography provides large fields of view images (several mm^2 compared to several hundred μm^2) with sub-micrometer spatial resolution. 3D image reconstructions are achieved using back propagation functions post-processing.

© 2020 Optical Society of America under the terms of the OSA Open Access Publishing Agreement

1. Introduction

Over the last decades, several major breakthroughs in the field of microscopy have been realized, targeting better and better spatio-temporal performances of various microscopy modalities: optical microscopy, fluorescence microscopy AFM, SEM, etc. Thanks to the large availability of lower cost, megapixel detectors and the progress in computing speeds in the 2000s, digital lensless imaging has emerged less than a decade ago. This technique has the advantage of being free from imaging optics, avoiding the drawbacks of aberrations, which otherwise systematically deteriorate the final image. Lensless microcopy has found wide applications in e.g. physics and biology [1–8]. The image formation is ensured by numerical reconstructions based mainly on Fourier optics. The experimental implementation is rather simple: a coherent beam illuminates the sample and the diffraction pattern is recorded on a CCD or CMOS camera. However, cameras are only sensitive to the intensity of the field (that is, its square modulus). The spatial phase is lost, making it impossible to directly retrieve the object from this measurement alone. One of the most common concept follows the first demonstration of Gabor's in-line holography in 1948, where a reference beam interferes with the diffracted beam and directly encodes the phase in the diffraction pattern [9]. The simplicity and ease of use make this lensless technique a promising method to investigate freely moving or static biological samples. Additionally, the revolutionary advances in microfabrication technologies have resulted in remarkable miniaturization of the imaging systems and have opened up a wide variety of innovative applications [10].

Thanks to its versatility as a non-invasive technique able to operate in a large field-of-view (FOV) [11] and high depth-of-field (DOF), this approach triggered strong interest for in vivo imaging applications. In most of the classical systems, there is a limitation of the FOV when

#380193 https://doi.org/10.1364/BOE.380193
Journal © 2020 Received 11 Oct 2019; revised 6 Feb 2020; accepted 6 Feb 2020; published 28 Apr 2020

Biomedical Optics EXPRESS

increasing the desired resolution; in other words, observing fine details of an object in a large field of view is extremely difficult. From the perspective of point-of-care (POC) applications, this constraint makes investigating biological samples more difficult, as they often have to be visualized in a large FOV, in e.g. 3D reconstruction of cell culture [12] or study of cell motility [13]. On the contrary, an outstanding characteristic of in-line holography lies in the possibility to reach rather large fields of view and close to wavelength spatial resolution.

Among all the advantages of in-line holography, the most important is the possibility to record the depth information the object in a single acquisition in contrast for example to tomography that requires hundreds of 2D projections. A 3D reconstruction of a volume object can thus be achieved from a single 2D hologram, with the possibility of retrieving both amplitude and phase information of the exit wave. This is therefore particularly advantageous for dynamical studies with contrast ensured by the refractive index of the various biological material.

In this paper, a microscope based on in-line holography is presented. We focused our work on in vivo high-resolution imaging in label free conditions. To illustrate the numerical 3D slicing, several measurements were performed using polymeric beads. The functionality of the system and a large variety of applications are then presented using several biological samples. A first demonstration of is performed on U2OS label free cells. Our primary tests were focused on the analysis of cells components as cytoplasm, nucleus, nuclear membrane and nucleolus, without the need of fluorescent labels. Additionally, in-vivo images of zebrafish embryos at various stages of evolution are showed answering to a list of questions for future improvements of the microscope. Finally, images and movies of live cyanobacteria were obtained. Real time analysis of bacteria motility is made possible thanks to the very low radiation dose needed to record a single hologram.

2. Materials and methods

2.1. Working principle

The lensless microscopy setup is composed of: an illumination source (a diode laser with adjustable power up to 60 mW, emitting at λ=405 nm, coupled to a polarization maintaining optical fiber (P1-405BPM-FC-2, Thorlabs)); a 1 µm diameter pinhole which is located in front of the fiber laser in order to increase the numerical aperture; and a CCD camera that collects the hologram (see Fig. 1). The wavelength was chosen to improve the spatial resolution, which is directly proportional to the illuminating wavelength. However, it could be adapted to match specific sample properties.

The spherical wave supplied by the coherent source illuminates the sample. The use of a pinhole allows creating a well-defined mode with improved spatial coherence that enhances the quality of the holograms. Part of the light field is diffracted by the sample, and interferes after propagation with the unscattered light, i.e. the holographic reference. The resulting hologram or diffraction pattern is collected by the CCD camera (ARTCAM-810KAI-USB3 Series with a 5.5 µm pixel size (P_{CCD}) and 3296 × 2472 pixels). The source and sample positions are controlled with motorized stages with nanometer scale step size. Downstream the holographic information is digitalized and processed. No optics are used to form the image of the object. The setup is compact (200 mm) and the working distance is about 40 mm. A "user friendly" interface has been implemented to ease sample manipulation and data acquisition (see supplementary material). The acquisition time (100 ms) and data processing (less than a second) are fast and the whole process can be performed in real time. The software allows recovering the morphological details of the sample in specific propagation planes.

Biomedical Optics EXPRESS

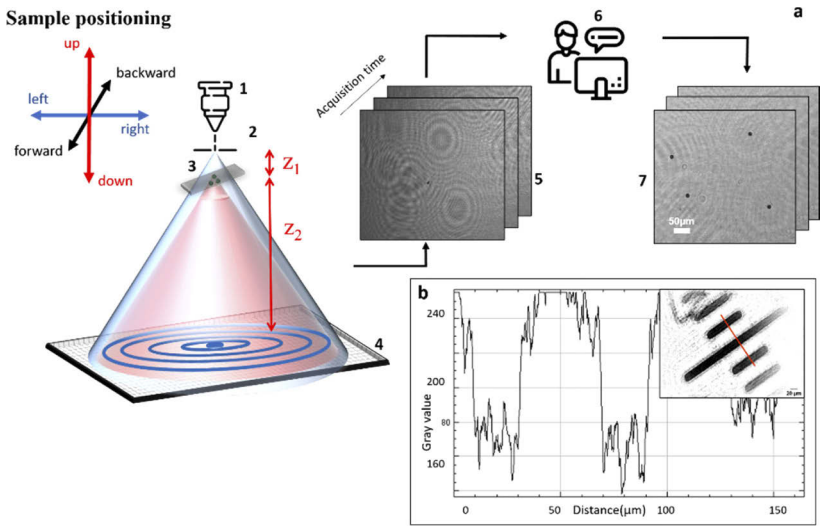

Fig. 1. a) Schematic representation of the principle. From left to right, holographic scheme showing the illumination source (1), the pinhole (2), the sample holder (3), and the imaging sensor (4). The holograms (5) are processed through fast algorithms (6) to retrieve the image of the object (7). b) Resolution test with an optical target. The graph is a lineout along the red line on the gray scale image, representing the holographic reconstruction of the sample.

2.2. Data acquisition parameters and processing

In our method, the magnification factor (M) is not given by an optical objective but by the following relation [14]:

$$M = \frac{z_2 + z_1}{z_1} \tag{1}$$

z_1 and z_2, as illustrated in Fig. 1, represent the source-sample and the sample-detector distances, respectively. In this demonstration, Z, the source-detector distance, is set at 40 mm and the sample is positioned at a variable distance between the point source and the imaging detector. However, the total working distance is constrained by the need of obtaining a certain degree of spatial coherence. Indeed, with most in-line configurations where a partial coherent light is supplied, a small (z_2) and a large (z_1) are used to increase the coherence though propagation [15–16]. In this case the magnification is close to 1. In our implementation, a highly coherent source is used and we are not limited to large z_1. However, there is an ideal compromise to reach high resolution: increasing z_2 increases M and the resolution, but for too high values of the sample-to-detector distance, the system numerical aperture limits the maximal recorded frequency and consequently limits the resolution [17]. The pinhole allows further increasing both the numerical aperture and the coherence of the source, thus enhancing the quality of the holograms. The power of the source is adjustable to optimize the dynamics of the data.

The digital hologram can be post-processed to increase the quality of the image reconstruction. In in-line holography, the loss of the diffracted field spatial phase during the detection stage symmetrizes the problem. Therefore, a virtual object, symmetrical to the real one, appears behind the detector. It is then impossible to reconstruct distinctly one object (the other one being out of focus and superimposed) [18–19]. This twin-image problem, inherent to this configuration, has to be solved. Here, we implemented an iterative algorithm based on the work of Latychevskaia and Fink [18]. Schematically, the hologram is first normalized by the reference signal, i.e. the signal on the CCD without any sample. The normalized hologram is then numerically propagated to a distance z_2 by a Fresnel propagator, where a real space constraint is applied. Here, it relies

Biomedical Optics EXPRESS

on the fact that the diffraction by the sample cannot create energy. Therefore, any pixel value greater than one is set to one. After back propagation to -z_2, the amplitude of the new hologram is replaced by the modulus square of the experimental hologram. After a limited number of iterations (typically between 10 and 20), the twin image contribution is effectively removed from the reconstructed image. It is thus possible to retrieve the sample physical parameters (transmittance and refractive index). Details on the algorithm can be found in Ref. [20]. The algorithm is available upon request to the authors.

The algorithm allows recovering both the amplitude and phase of the exit wave. Therefore, it is possible to create a 3D image by "slicing" the samples through numerical back propagation at different depths. Moreover, this requires only one hologram recorded in a single acquisition. To demonstrate the 3D imaging capability of the instrument, we carried out test experiments using synthetic samples (polymeric microspheres) arranged in a controlled 3D scheme. The sample is presented in Fig. 2(b)–(c). For this experiment, we used 3 stacked layers of optical glass with individual thickness of approximatively 130 µm. Between these layers we distributed a solution of deionized water with a concentration of 0.06 µL of polymeric targets with diameter $d = 10$ µm. The total working distance is $Z = z_1 + z_2 = 40$ mm. The sample was positioned at $z_1 = 3$ mm. Using the digital propagation function, i.e. numerically varying z_2, we can recover several focal planes (see Fig. 2), effectively retrieving the microscope slides thicknesses. As clearly visible in Fig. 2(b), the different microspheres in the color frames are in focus for different values of z_2, reflecting their vertical position in the slice multi-layer. Typically, in classical microscopy the DOF is inversely proportional to the numerical aperture and magnification of the objective [21]. The limitation is less stringent in in-line holography; however, the complexity of the sample is an important parameter. Indeed, a thick and complex sample limits the DOF due to the high scattering and absorption of the sample that causes losses of information. Several methods have been developed to improve the optical quality of some biological targets that could advantageously be applied to in-line holography [22–23].

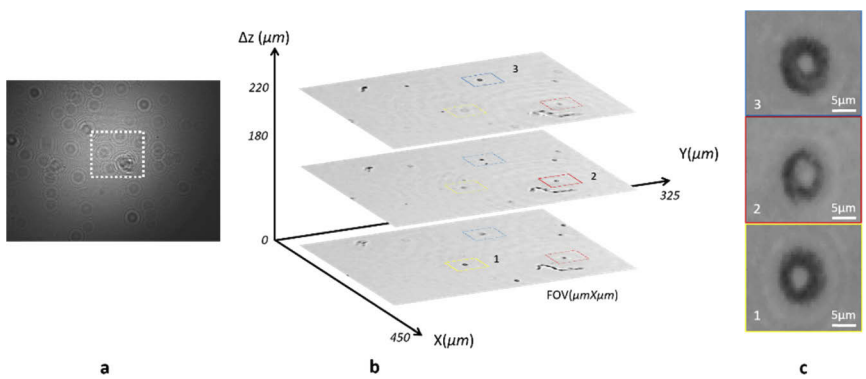

Fig. 2. Reconstructed amplitude of the polymeric beads using the slicing function, using a single hologram acquisition; a) The hologram in full FOV, b) the reconstruction in the 3 sample planes and c) zoom for each plane, corresponding to a microsphere retrieved "in-focus". The total sample thickness is of 250 µm.

The achievable lateral resolution in in-line holography has been subject to many studies. A detailed discussion can be found, for instance, in Ref. [24]. The theoretical lateral resolution is defined by $\delta_{lat} = \lambda/2NA$ where NA is the numerical aperture of the beam, and λ the wavelength. In in-line holography, NA is defined as $NA = D/Z$ with D the beam size at the detector plane.

Here, we have used instead the Rayleigh criterion, which defines the experimental spatial resolution R as the shortest distance required to distinguish two point sources [25]. It can be

Biomedical Optics EXPRESS

expressed as

$$R = n_{10\%-90\%}\ \Delta_{pixel} \tag{2}$$

with $n_{10\%-90\%}$ the number of pixels that constitute the 10% - to - 90% rising (or falling) edge, in intensity, and Δ_{pixel} the image pixel size. We have used an optical target to define the experimental resolution and obtained an experimental lateral resolution of R_{exp} = 1.4 µm (see inset Fig. 1(b)). In the inset of Fig. 1(b) the total FOV is 300 µm in diameter and corresponds to a magnification factor M = 60.

2.3. Sample preparation

2.3.1. Cell culture

U2OS cells were cultured in Dulbecco's modified Eagle's medium (DMEM, ThermoFisher, 31966021), supplemented with 10% fetal bovine serum (FBS) (Sigma, F7524) and 5% penicillin/streptomycin (Gibco, 15140122) at 37°C and 5% CO2. For microscopy, cells were grown on 12 mm round coverslips N°1,5H (Marienfeld, 900532), fixed in 2% formaldehyde (Thermo Scientific, 28908) for 20 min at 37°C and rinsed with PBS before mounting in DAKO Fluorescence mounting medium (S3023).

2.3.2. Zebrafish embryos

Wildtype zebrafish (Danio rerio) of the AB strain were maintained in accordance with institutional guidelines. Embryos were obtained from natural spawning and staged according to Kimmel et al [26]. Imaging: At given stages (6, 24 or 48 hours post fertilization (hpf)), embryos were collected and dechorionated for in-vivo imaging. Before imaging, they were anesthetized with 0.2 mg/ml tricaine (MS-222, Sigma) then placed in the well of a glass-bottom microfluidic chip.

2.3.3. Cyanobacteria: strains and culture conditions

The freshwater cyanobacterium Synechocystis sp. PCC 6803 wild type were grown photoautotrophically in a modified BG11 medium (Herdman et al., 1973), containing twice amount of sodium nitrate. Cells were kept in a rotary shaker (120 rpm) at 30°C and illuminated by fluorescent white lamps giving a total intensity of about 50 to 60 mmol photons m^{-2} s^{-1} under a CO_2 atmosphere. The cells were maintained in the logarithmic phase of growth and were collected at an optical density at 800 nm of 0.6 to 0.8 [27].

3. Results and discussion

3.1. 3D reconstruction of U2OS cell culture

Using our lensless microscope, we collected holograms of U2OS cells at various distances between source and image sensor and various magnification factors, and processed them as described above. The reconstruction steps are presented in Fig. 3: from hologram to standard reconstruction and twin image corrected reconstruction. All images were acquired in a single 100 ms acquisition time. The reconstruction time could vary from few seconds to several minutes depending of the number of successive planes required and the size of the selected hologram area.

In Fig. 3(b) the full FOV (80mm^2) of the mounted sample is presented. Two regions of interest were selected for this study (Fig. 3(a, c)). The first region (Fig. 3(a, d, g)) presents an area with a single cell. In this reconstruction the magnification factor is about M = 36. Figure 3(c, f, i, h) report a larger FOV containing several cells and a factor M = 40. In both region of analysis, we distinguish several areas of the cell, e.g. (Fig. 3(g)): cytoplasm (A), nuclear envelope (C), and the nucleolus (B). The size of the reconstructed cells, as well as their nuclear dimensions, are consistent with the sizes of freely growing U2OS cells reported in the literature [28]. Additionally, the images are well contrasted and contain both the amplitude and the phase

Biomedical Optics EXPRESS

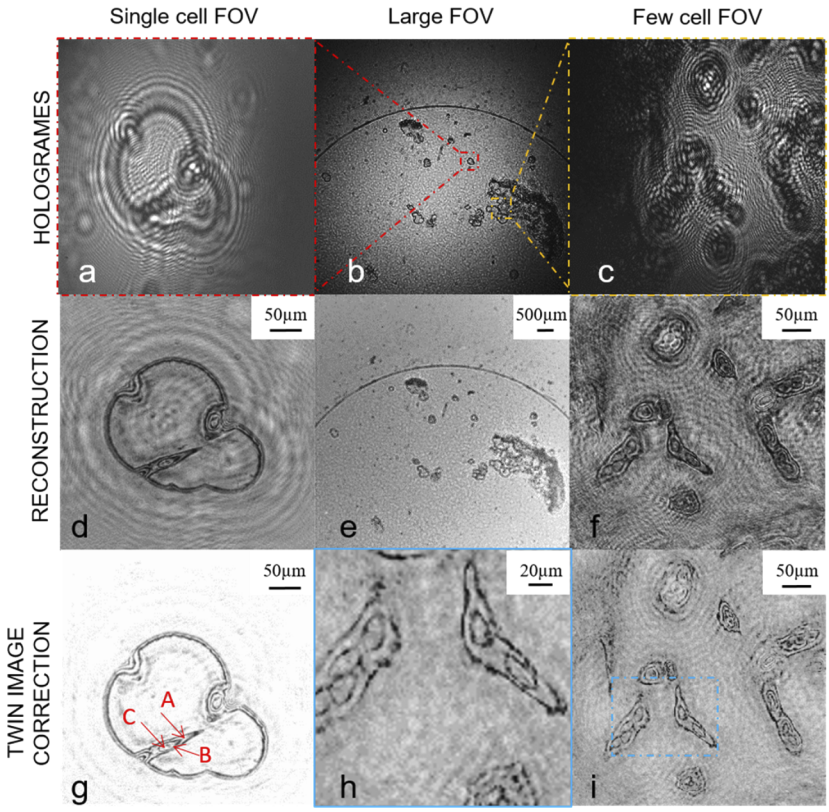

Fig. 3. a), b), c) Holograms, d), e), f) Reconstructed amplitude image of cell culture with acquisition software and no twin image correction g), h), i) Reconstructed amplitude image using post-processing data with twin image correction; h) is a zoom into the blue square represented in i). The capital letters corresponds to cytoplasm (A), nuclear envelope (B), and the nucleolus (C).

of the exit wave, which open the possibility of numerically implementing any imaging technique. We have to mention that the magnification factor is changed both through numerical and physical manipulation (changing the position of the sample by changing the distance z_1).

In this scheme, the resolving power R_{exp} increases with the magnification factor M. For example, Fig. 3-e shows a large FOV with $M = 2$ and $R_{exp} = 24\,\mu m$. Our device allows to easily zoom in a given area, as reported in Fig. 3-d, simply by tuning the vertical sample position. As an illustration, Fig. 3(e) represents a zoom into the red square (Fig. 3(b)) with a magnification factor $M = 36$ and a resolving power $R_{exp} = 0.8\,\mu m$. The calculation of the effective spatial resolution is illustrated in Fig. 4, applying the Rayleigh criterion. Several points were chosen, and the final value was estimated as an average of the measured values. We obtain from the nuclear envelope a resolution of 0.6 µm with a pixel size of $\Delta_{pixel} = 0.15\mu m$.

Using the unique 3D imaging capability of our microscope, we can give an estimate of the thickness of the sample (Fig. 5); to simplify, we start at z_2=0 as arbitrary starting position for the fine numerical scanning over several longitudinal plane. We clearly observe that the nucleus shape evolves over an 8 µm propagation range, as seen Fig. 5 where the nuclear size varies from 8 to 11 µm. Using a 3D slicing package from the Image J software suite, we have compiled the displayed slices to achieve a 3D representation of the sample, which is available in the

Biomedical Optics EXPRESS

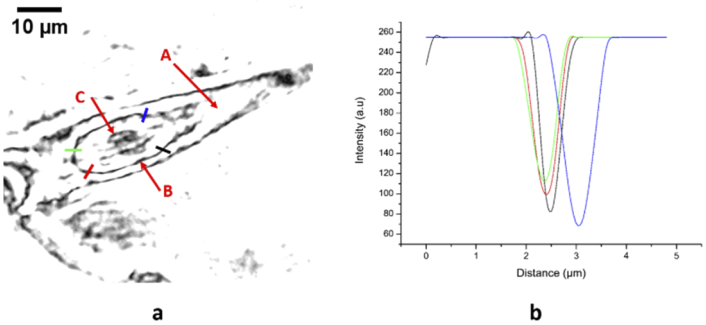

Fig. 4. Estimation of the resolution on the nuclear envelope: a) the sample and the region chosen for calculation taken from Fig. 3(g). The capital letters corresponds to cytoplasm (A), nuclear envelope (B), and the nucleolus (C); b) profile plots of the region marked in **a**.

supplementary material (movie). The 3D rendering is satisfying but we notice that the depth resolution (theoretically of 700 nm) limits the quality of the Z perception.

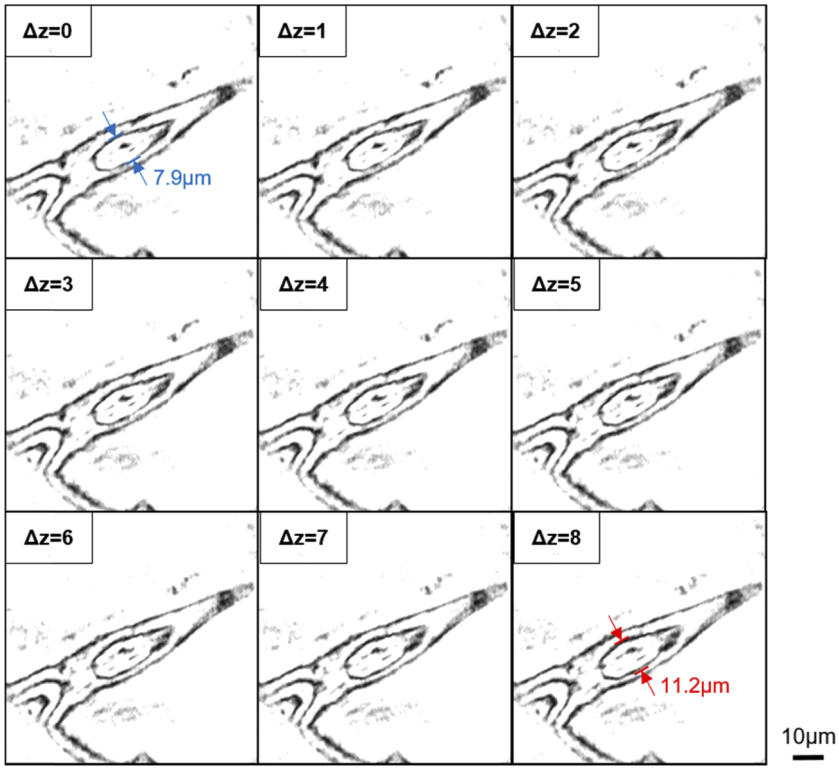

Fig. 5. Slicing of the reconstructed amplitude of the cell displayed in Fig. 4(a). The slices are recovered at different focal points Z_i (µm) ranging from 0 to 8 µm (see Visualization 1).

3.2. In-vivo analysis of cyanobacteria motility (synechocystis PCC 6803)

The low dose of light, spread over the large FOV, allows the system to be compatible with in vivo analysis. In this section, we focus our lensless microscope on cyanobacteria cells (Synechocystis), a high-aimed type of cells. Studying this kind of cell is challenging due to their fast motility

Biomedical Optics EXPRESS

and strong interaction with light. The accessibility of a large FOV allowed us to analyze the cells behavior and their interaction with a probe light [29]. This micro-organism, according to several studies, use micro-optics to sense light direction. To study this dynamics, a second diode ($\lambda = 637$ nm) was inserted in the system. The short acquisition time needed to record for a complete hologram allows generating a fast stroboscopic sequence compiled in a live movies. This allow studying the cells motion in real time.

Figure 6 presents amplitude and phase reconstructions of living cyanobacteria. Within each cell, the bright point (visible in both amplitude and phase maps) is associated to a self-focusing effect of the light propagating through the cell. The cyanobacteria used in our experiment are spherically shaped. As a result, similarly to the human eye, they can focus light to the rear side of the cell which appears the brightest. The motility is ensured by pili that are photo-activated only in the regions where light is concentrated [30]. The ability to move help cyanobacteria to orientate and move favorably to light and environment.

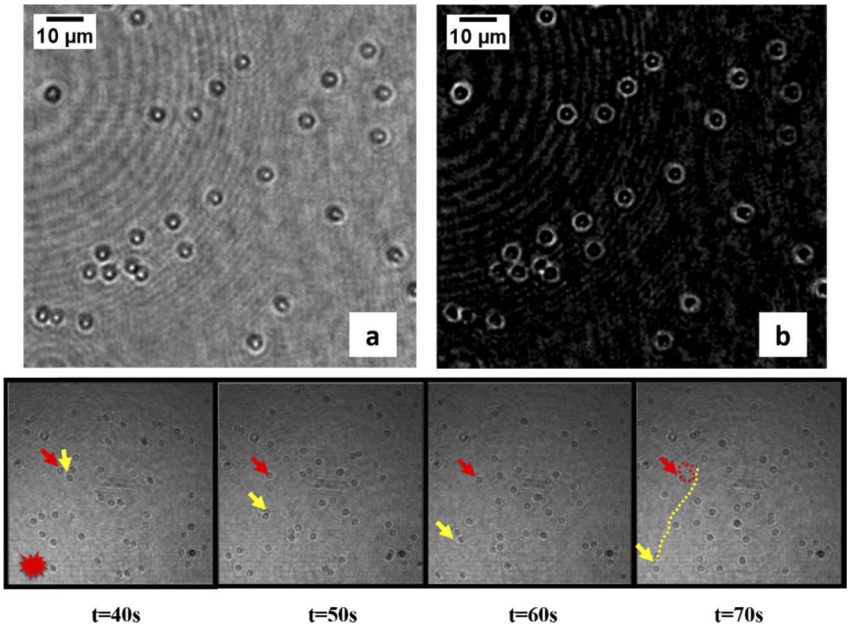

Fig. 6. Reconstructed hologram from cyanobacteria, in a) amplitude and b) phase. Bottom line: screenshots at different times that show the movement of the cells in the fluid in the direction of the source of light (the red star). In a and b, the scale bar 5 µm (see Visualization 2).

From Fig. 6, we can calculate the motility of a single cell. We found a motility ranging between 0.03 and 0.07 µm/s, in good agreement with previous studies [31]. In our experiments, we observed that the majority of the cells (70%) moved towards the light (for example see the yellow trajectory in Fig. 6). The rest (30%) displayed a stationary behavior followed by a circular rotation (red arrow from Fig. 6). Dead cells were not considered and the motility estimation was made for a total of 40 cells that are present in the screen captures in Fig. 6. The acquisition time for individual frames was 100 ms.

3.3. Thick sample and perspectives

Imaging biological samples depends on the index of refraction (n). This can be an issue for thick samples. In this last study, we examined the capability of our system to capture images of live zebrafish embryos at various stages of their development (Fig. 7(a–g)). The hologram

Biomedical Optics EXPRESS

acquisitions were performed by replacing the pinhole by a 0.60 NA lens to create a spherical wave in order to increase the signal. The image reconstructions were performed similarly to the procedures presented in the sections above. A zebrafish embryo is a three-dimensional object, thus reconstructions at different depths using our microscope allow recovering z-slices of the sample, in order to focus on different part components or to follow the 3D structure of one (see Fig. 7). As an illustration, the morphology of a blood vessel superimposed with bone structure (Fig. 7(g, f)) within the tail fin (Fig. 7(a, c, d)) and the shape of the caudal fin are presented. In Fig. 7-(d) we choose to define a relative position $Z = 0\,\mu m$ where the red arrow indicates a bone structure line; for Fig. 7–(e) the new distance from the relative position is $Z_1 = 250\,\mu m$ and the arrow indicates the caudal fin; in g at $Z_2 = 500\,\mu m$ two main blood vessels are indicated by the red line vein and artery while for f at same distance $Z_2 = 500\,\mu m$ the red lines are following the direction of intersegmental blood vessels.

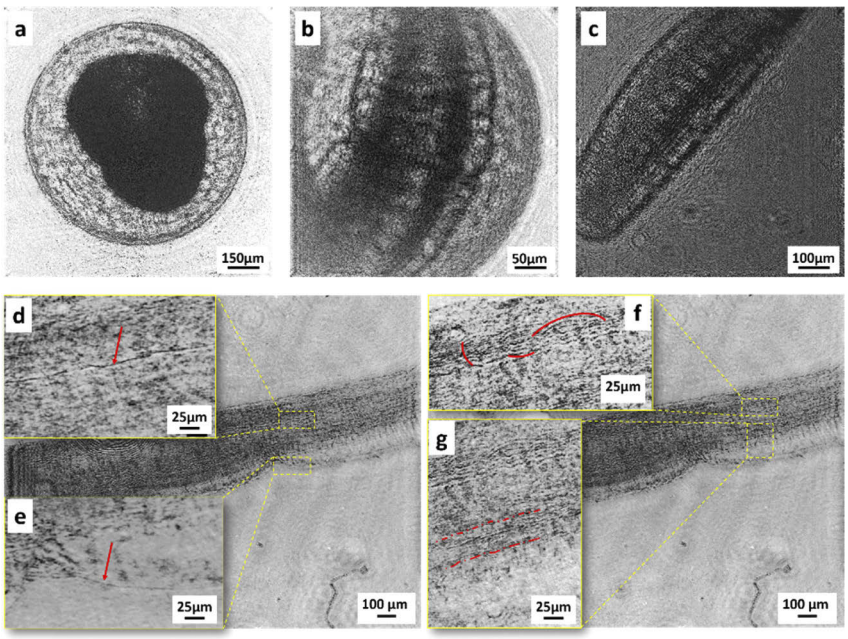

Fig. 7. a) 6 hpf full zebrafish embryo, b) Detail of a 24 hpf zebrafish embryo, c) Detail of a 48 hpf dechorionated embryo, H) Reconstructed amplitude image of a dechorionated 48 hpf zebrafish embryo and corresponding zooms of different details: d) Relative position $Z = 0\,\mu m$, the red arrow is a bone structure line, e) $Z_1 = 250\,\mu m$ the arrow indicates the caudal fin; g) $Z_2 = 500$ the red lines are following the direction of intersegmental blood vessels, while in f) at same distance $Z_2 = 500\,\mu m$ the red line points the vein and artery. The given values of Z_i correspond to the relative backpropagation distance, i.e. to the relative distance between the transverse slices.

However, complex refractive index variations within the sample scatter the photons and distort the optical wavefront, resulting in an increased background noise and a reduced quality of the images. Nevertheless, several approaches have been proposed for cleaning that could achieve better results for zebrafish analysis [32]. Another solution would be to use digital holography in an off-axis configuration, in which the reference wave does not propagate inside the sample medium [33].

Biomedical Optics EXPRESS

4. Conclusion

Lensless imaging based on in-line holography is an appealing solution for biomedical investigations due to its portability and in-vivo capability. We imaged and analyzed biological samples in different working conditions, pointing out the ease of use of our platform for real time in vivo studies. This non-invasive tool provides a wide range of applications from single cell to population of cells and tissue imaging. Another remarkable advantage is the low level of radiation that is needed, as the illumination is spread over the full FOV and the laser power is small. In the first configuration we presented, the total power received by the sample is 0.25nW for a distance fiber-pinhole of 2 mm.

The instrument is compact, cost-effective and allows sub-micrometer spatial resolution associated to a wide FOV. A major advantage of in-line holography is that it is label free. Moreover, after eliminating the twin image, it provides the exit field complete information, i.e. amplitude and phase. Consequently, it is possible to observe 3D samples with phase contrast. The fast acquisition time (100 ms) allows to study 3D dynamical properties of cells. As an illustration, we reported the monitoring of the motility of cyanobacteria excited by light. Indeed, for live analysis, back propagation functionalities have been embedded in our software to recover through slicing the 3D shape of cells or tissues. We could observe very rapidly small features, thanks to the high speed of the process. Our in-line configuration allows for the observation of larger features (FOV between 15 mm and 400 µm), at a variable resolution (24 µm to 0.8 µm). Additionally, it differs from common on chip digital in-line holography (DILH) setups by the large sample-to-CCD distance [34], which allows implementing supplementary tools for specific applications, illustrated here by the addition of a second light source to study the photokinesis response of cyanobacteria. Additional optical elements, such as filters or polarizers, could also be inserted before the detector to clean the hologram from parasitic contributions. DILH in collimated beam configuration, which presents similar flexibility, imposes however a fixed FOV and magnification [35]. Our setup, on the other hand, allows modifying easily the magnification factor of the microscope, increasing accordingly the spatial resolution. Compared with an off-axis digital holography microscopy, in-line holography is very stable against vibration of the optical system, sharing the advantages of portability allowing this system to be brought out of the laboratory without requiring any isolation system. A forthcoming and more sophisticated setup aims at integrating single cell manipulation.

Funding

H2020 Future and Emerging Technologies (665207, 829153); European laser research infrastructure (LASERLAB-EUROPE) (654148); Agence Nationale de la Recherche; CEA/DRF Impulsion - NanoBiom; Défi “IMAG’IN”CNRS; Région ile de France-DIM ELICIT (grant IMAChip); Technologie et à la Recherche en Essonne (ASTRE) -“NanoLight"; Centre National de la Recherche Scientifique.

Acknowledgement

We acknowledge support from the CEA/DRF Impulsion program with the grant “NanoBiom”, Défi “IMAG’IN”CNRS grant program “Nano-bio-4D. We acknowledge support from Région Ile de France through the DIM ELICIT program, grant IMAChip and the Action de Soutien à la Technologie et à la Recherche en Essonne (ASTRE) program through the “NanoLight” project. We acknowledge financial support from the European Union through the Future and Emerging Technologies (FET) Open H2020: VOXEL (grant 665207) and PETACom (grant 829153) and the integrated initiative of European laser research infrastructure (LASERLAB-EUROPE) (grant agreement no. 654148). Support from the French ministry of research through the 2013 Agence Nationale de Recherche (ANR) grants “NanoImagine”, 2014 “ultrafast lensless

Biomedical Optics EXPRESS

Imaging with Plasmonic Enhanced Xuv generation (IPEX)", 2016 "High rEpetition rate Laser for Lensless Imaging in the Xuv (HELLIX)"; from the DGA RAPID grant "SWIM", from the CentreNational de Compétences en Nanosciences (C'NANO) research program through the NanoscopiX grant; the LABoratoire d'EXcelence Physique Atoms Lumière Matière -LABEX PALM (ANR-10-LABX-0039-PALM), through the grants "Plasmon-X" and "HIgh repetition rate Laser hArmonics in Crystals (HILAC)" are acknowledged

We thank Fernando Muzzopappa and Institut de Biologie Intégrative de la Cellule (I2BC) for the biological support and for the opportunity to use the of cyanobacteria in our experiments.

Disclosures

The authors declare no conflicts of interest.

References

1. J. Wu, G. Zheng, and L. M. Lee, "Optical imaging techniques in microfluidics and their applications," Lab Chip **12**(19), 3566 (2012).
2. X. Zhang, I. Khimji, U. A. Gurkan, H. Safaee, P. N. Catalano, H. O. Keles, E. Kayaalpb, and U. Demirci, "Lensless imaging for simultaneous microfluidic sperm monitoring and sorting," Lab Chip **11**(15), 2535–2540 (2011).
3. S. Witte, V. T. Tenner, D. W. E. Noom, and D. W. E. Noom, "Lensless diffractive imaging with ultra-broadband table-top sources: from infrared to extreme-ultraviolet wavelengths," Light: Sci. Appl. **3**(3), e163 (2014).
4. O. Mudanyali, E. McLeod, W. Luo, A. Greenbaum, A. F. Coskun, Y. Hennequin, C. P. Allier, and A. Ozcan, "Wide-field optical detection of nanoparticles using on-chip microscopy and self-assembled nanolenses," Nat. Photonics **7**(3), 247–254 (2013).
5. M. Mihailescu, E. I. Scarlat, I. A. Paun, I. Grigorescu, R. Radu, and O. T. Nedelcu, "Empirical quantitative characterization of holographic phase images of normal and abnormal cervical cells by fractal descriptors," Comput. Methods Biomech. Biomed. Eng. Imaging Vis. **6**(4), 386–395 (2018).
6. V. Calin, M. Mihailescu, N. Mihale, A. Baluta, E. Kovacs, T. Savopol, and M. Moisescu, "Changes in optical properties of electroporated cells as revealed by digital holographic microscopy," Biomed. Opt. Express **8**(4), 2222–2234 (2017).
7. D. Donnarumma, A. Brodoline, D. Alexandre, and M. Gross, "Blood flow imaging in zebrafish by laser doppler digital holography," Microsc. Res. Tech. **81**(2), 153–161 (2018).
8. E. Mathieu, C. D. Paul, R. Stahl, G. Vanmeerbeeck, V. Reumers, C. Liu, K. Konstantopoulos, and L. Lagae, "Time-lapse lens-free imaging of cell migration in diverse physical microenvironments," Lab Chip **16**(17), 3304–3316 (2016).
9. D. Gabor, "A new microscopic principle," Nature **161**(4098), 777–778 (1948).
10. V. Bianco, B. Mandracchia, V. Marchesano, V. Pagliarulo, F. Olivieri, S. Coppola, M. Paturzo, and P. Ferraro, "Endowing a plain fluidic chip with micro-optics: a holographic microscope slide," Light: Sci. Appl. **6**(9), e17055 (2017).
11. W. Luo, Y. Zhang, A. Feizi, Z. Göröcs, and A. Ozcan, "Pixel super-resolution using wavelength scanning," Light: Sci. Appl. **5**(4), e16060 (2016).
12. B. W. Graf and S. A. Boppart, "Imaging and analysis of three-dimensional cell culture models "," Methods Mol. Biol. **591**, 211–227 (2010).
13. D. Nakane and T. Nishizaka, "Asymmetric distribution of type IV pili triggered by directional light in unicellular cyanobacteria," Proc. Natl. Acad. Sci. U. S. A. **114**(25), 6593–6598 (2017).
14. A. Pogany, D. Gao, and S. W. Wilkins, "Contrast and resolution in imaging with a microfocus x-ray source," Rev. Sci. Instrum. **68**(7), 2774–2782 (1997).
15. Y. Wu and A. Ozcan, "Lensless digital holographic microscopy and its applications in biomedicine and environmental monitoring," Methods **136**, 4–16 (2018).
16. O. Mudanyali, D. Tseng, C. Oh, S. O. Isikman, I. Sencan, W. Bishara, C. Oztoprak, S. Seo, B. Khademhosseinia, and A. Ozcan, "Compact, light-weight and cost-effective microscope based on lensless incoherent holography for telemedicine applications," Lab Chip **10**(11), 1417–1428 (2010).
17. N. Verrier, C. Fournier, A. Cazier, and T. Fournel, "Co-design of an in-line holographic microscope with enhanced axial resolution: selective filtering digital holography," J. Opt. Soc. Am. A **33**(1), 107–116 (2016).
18. T. Latychevskaia and H. W. Fink, "Solution to the Twin Image Problem in Holography," Phys. Rev. Lett. **98**(23), 233901 (2007).
19. B. K. Chen, T. Y. Chen, S. G. Hung, S. L. Huang, and J. Y. Lin, "Twin image removal in digital in-line holography based on iterative inter-projections," Opt. Laser. Eng. **51**(5), 553–559 (2013).
20. PhD Thesis Julien Samaan (2016) https://www.theses.fr/198731868
21. C. Demant, B. Streicher-Abel, and P. Waszkewitz, *Industrial Image Processing: Visual Quality Control in Manufacturing* (Springer, 1999)

Biomedical Optics EXPRESS

22. Y. Zhang, Y. Shin, K. Sung, S. Yang, H. Chen, H. Wang, D. Teng, Y. Rivenson, R. P. Kulkarni, and A. Ozcan, "3D imaging of optically cleared tissue using a simplified CLARITY method and on-chip microscopy," Sci. Adv. **3**(8), e1700553 (2017).
23. Y. Wu, Y. Rivenson, Y. Zhang, Z. Wei, H. Günaydin, X. Lin, and A. Ozcan, "Extended depth-of-field in holographic imaging using deep-learning-based autofocusing and phase recovery," Optica **5**(6), 704–710 (2018).
24. S. Jericho, J. Garcia-Sucerquia, W. Xu, M. Jericho, and H. Kreuzer, "Submersible digital in-line holographic microscope," Rev. Sci. Instrum. **77**(4), 043706 (2006).
25. D. T. Attwood, *Soft x-rays and Extream Ultraviolet Radiation* (Cambridge University Press, 1999).
26. C. B. Kimmel, W. W. Ballard, S. R. Kimmel, B. Ullmann, and T. F. Schilling, "Stages of embryonic development of the zebrafish," Dev. Dyn. **203**(3), 253–310 (1995).
27. M. Herdman, S. F. Delaney, and N. G. Carr, "A new medium for the isolation and growth of auxotrophic mutants of the blue-green alga Anacystis nidulans," J. Gen. Microbiol. **79**(2), 233–237 (1973).
28. B. Koch, S. Sanchez, C. K. Schmidt, A. Swiersy, S. P. Jackson, and O. G. Schmidt, "Confinement and deformation of single cells and their nuclei inside size-adapted microtubes," Adv. Healthcare Mater. **3**(11), 1753–1758 (2014).
29. N. Schuergers, T. Lenn, R. Kampmann, M. V. Meissner, T. Esteves, M. Temerinac-Ott, J. G. Korvink, A. R. Lowe, and C. W. Mullineaux, "Cyanobacteria use micro-optics to sense light direction," eLife **5**, e12620 (2016).
30. B. A. Whitton and M. Potts, "The Ecology of Cyanobacteria: Their Diversity in Time and Space," J. Paleolimnol. **28**(3), 383–384 (2002).
31. A. Wilde and C. W. Mullineaux, "Motility in cyanobacteria: polysaccharide tracks and Type IVpilus motors," Mol. Microbiol. **98**(6), 998–1001 (2015).
32. D. Donnarumma, A. Brodoline, D. Alexandre, and M. Gross, "4D holographic microscopy of zebrafish larvae microcirculation," Opt. Express **24**(23), 26887–26900 (2016).
33. J. Gao, J. A. Lyon, D. P. Szeto, and J. Chen, "In vivo imaging and quantitative analysis of zebrafish embryos by digital holographic microscopy," Biomed. Opt. Express **3**(10), 2623–2635 (2012).
34. H. Zhu, S. O. Isikman, O. Mudanyali, A. Greenbauma, and A. Ozcan, "Optical imaging techniques for point-of-care diagnostics," Lab Chip **13**(1), 51–67 (2013).
35. V. Dyomin, A. Gribenyukov, A. Davydova, M. Zinoviev, A. Olshukov, S. Podzyvalov, I. Polovtsev, and N. Yudin, "Holography of particles for diagnostics tasks [Invited]," Appl. Opt. **58**(34), G300 (2019).